Research Article

High temperature mechanical retention characteristics and oxidation behaviors of the MoSi₂(Cr₅Si₃)–RSiC composites prepared via a PIP–AAMI combined process

Peng-zhao GAO[a,b,c,*], Lei CHENG[a,b,c], Zheng YUAN[a,b,c],
Xiao-pan LIU[a,b,c], Han-ning XIAO[a]

[a]*College of Materials Science and Engineering, Hunan University, Changsha 410082, China*
[b]*Hunan Province Key Laboratory for Advanced Carbon Materials and Applied Technology, Hunan University, Changsha 410082, China*
[c]*Hunan Province Key Laboratory for Spray Deposition Technology and Application, Hunan University, Changsha 410082, China*

Abstract: In the present paper, $MoSi_2(Cr_5Si_3)$–RSiC composites were prepared via a combination of precursor impregnation pyrolysis (PIP) and $MoSi_2$–Si–Cr alloy active melt infiltration (AAMI) process. Composition, microstructure, mechanical retention characteristics, and oxidation behaviors of the composites at elevated temperature were studied. X-ray diffraction (XRD) pattern confirms that the composites mainly compose of 6H–SiC, hexagonal $MoSi_2$, and tetragonal Cr_5Si_3. Scanning electron microscopy (SEM) image reveals that nearly dense $MoSi_2(Cr_5Si_3)$–RSiC composites exhibiting three-dimensionally (3D) interpenetrated network structure are obtained when infiltrated at 2173 K, and the interface combination of the composites mainly depends on the composition ratio of infiltrated phases. Oxidation weight gain rate of the composites is much lower than that of RSiC matrix, where MoSiCr2 possesses the lowest value of 0.1630 mg·cm^{-2}, about 78% lower than that of RSiC after oxidation at 1773 K for 100 h. Also, it possesses the highest mechanical values of 139.54 MPa (flexural strength σ_f and RT) and 276.77 GPa (elastic modulus E_f and RT), improvement of 73.73% and 29.77% as compared with that of RSiC, respectively. Mechanical properties of the composites increase first and then decrease with the extension of oxidation time at 1773 K, due to the cooperation effect of surface defect reduction via oxidation reaction and thermal stress relaxation in the composites, crystal growth, and thickness increase of the oxide film. Fracture toughness of MoSiCr2 reaches 2.24 MPa·m$^{1/2}$ (1673 K), showing the highest improvement of 31.70% as compared to the RT value.

Keywords: $MoSi_2(Cr_5Si_3)$–RSiC composites; precursor impregnation pyrolysis and $MoSi_2$–Si–Cr alloy active melt infiltration (PIP–AAMI); high temperature mechanical characteristic; oxidation behavior

* Corresponding author.
E-mail: gaopengzhao7602@hnu.edu.cn

1 Introduction

Re-crystallized silicon carbide (RSiC) is well-known for its excellent creep resistance, high strength, high hardness, oxidation resistance, chemical stability at elevated temperature, high thermal conductivity, relatively low coefficient of thermal expansion, and low density [1,2]. It has been receiving attention as materials for load-bearing and electrical-heating parts at high temperature, thermal exchanger, hot gas particulate filters, and reactor, etc. [1,3–5].

RSiC does not shrink during its re-crystallization process at about 2573 K because of the evaporation–condensation mechanism, which results in a three-dimensionally (3D) interconnected porous structure [2,6]. The interconnected porous structure severely reduces the mechanical, thermal, and electronic properties, as well as to the high-temperature oxidation resistance of RSiC itself. What's more, the lower oxidation resistance of RSiC degrades other properties such as mechanical, electrical properties, and acutely reduces the service life [2,6,7] when it works at high-temperature oxidation condition.

Recently, a new type of ceramic-metal composite, in which both phases are continuous and 3D interpenetrating in the whole microstructure, has drawn considerable attention [8,9]. This kind of composites exhibits multi-functions for their special structure and remaining performance of each phase; the most general method for fabricating these composites is to impregnate the desired phases into the pre-existing open-cell porous preform, thereby producing the requisite connectivity and spatial distribution of two or more phases [1,10].

The main purpose of this study is to prepare a dense RSiC matrix composite exhibiting a 3D interpenetrated network structure by filling up the pores of the matrix with an infiltrator, which possesses excellent high-temperature oxidation resistance. The target composites would combine the excellent creep resistance and high strength of RSiC matrix with the excellent high-temperature oxidation resistance of the infiltrator. According to the previous studies, metal silicides ($MoSi_2$, Cr_5Si_3, and Ti_5Si_3, etc.) are good candidates [11–14].

The method of melt infiltration has been reported by many researchers on either molten silicon, silicon metal alloy, or metal disilicides via the infiltration or reactively infiltration into the porous preforms of C, SiC, or SiC+C, etc. [15–19]. Novakovic *et al*. [20], Xu [21], Roger *et al*. [22], and Jiang *et al*. [23] performed the thermodynamics calculation on the corresponding reaction occurred during infiltrated process. Calderon *et al*. [24], Caccia *et al*. [25], and Voytovych *et al*. [26] studied the wetting properties between the infiltrated phase and matrix. These references proved the feasibility of the abovementioned process.

While the high melting point of metal silicides (most are above 2273 K) and the poor interface combination between infiltrated phase and RSiC matrix prevent the further research on RSiC matrix composites [1]. Xie *et al*. [2] also try to improve the interface combination using precursor impregnation pyrolysis and melt infiltration (PIP–MI) combined process, while the expensive precursor (polycarbosilane, PCS) and higher infiltrated temperature (at about 2323 K) limit the application of the obtained composites.

Meier and Heinrich [27] reported the use of $MoSi_2$ alloy ($MoSi_2$–Si–X (X = Cr, Ti, Al, etc.)) activated melting infiltration method to produce the $MoSi_2$–SiC composite at a lower temperature (below 2073 K), in which SiC+C green body works as the matrix. The obtained composites exhibit excellent mechanical properties at room and elevated temperatures. In this infiltrated system, Si (low melting point, 1683 K) helps to reduce the infiltrated temperature via the formation of uniform pre-melted alloy, and the excessive Si can react with X or existed C to form the metal silicide and SiC to avoid the decline of high-temperature mechanical properties of the composites under oxidation surroundings [27,28].

In this paper, PIP (phenol formaldehyde resin, PF)–AAMI ($MoSi_2$–Si–Cr) combined process was adopted to prepare dense $MoSi_2$–RSiC composites. The composition, microstructure, mechanical retention characteristics, and oxidation behaviors of the composites at elevated temperature were studied. Several interesting results were obtained.

2 Experimental

2.1 Raw materials

RSiC was commercially obtained from Fawcett Technology Ceramic Industry Co., Ltd. Its porosity and volume density equaled to 18.62% and 2.61 g·cm^{-3}, and its flexural strength and elasticity modular were 80.32 MPa and 213.27 GPa, respectively. Silicon (Si) and chromium (Cr) powders were commercially obtained from Zhongnuo New Materials Co., Ltd., Beijing, China, with

a purity of 99.0%. Phenol formaldehyde resin (2130#) was commercially obtained from Zhida Insulation Chemical Co., Ltd., Changsha, China. $MoSi_2$ powder ($MoSi_2 > 99.5\%$) was commercially obtained from Zhengzhou Songshan Heating Elements Co., Ltd., Zhengzhou, China. The composition of pre-melted alloy powder was designed according to Ref. [29] and is listed in Table 1.

2. 2 Preparation of the $MoSi_2(Cr_5Si_3)$–RSiC composites

2.2.1 Alloy powder pre-melt process

Different ratios of $MoSi_2$, Si, and Cr powders were weighted according to the compositions listed in Table 1, the mixture powder was ball milling and was pressed into disks, then the disks were heated to 1673 K for 1–2 h at the rate of 10 $K \cdot min^{-1}$ to obtain pre-melted alloy blocks with uniform compositions [30,31].

2.2.2 PIP process

PIP process was performed to obtain pyrolytic C (PyC) layer on the inner surface of RSiC matrix, and the thickness of PyC layer was controlled via controlling the PIP cycles when RSiC was employed as the preform and PF as the organic precursor [31,32]. Detailed PIP processes were as follows: RSiC preform was located in an autoclave and then heated to 303 K. When the autoclave was vacuumized less than 0.01 MPa, the diluted solution of PF in ethanol (50% v/v) at 303 K was injected into the autoclave until the preform was completely submerged in PF solution and then dwelled at this pressure for 2 h. Subsequently, the PF solution covered preform was subjected to 0.8 MPa and dwelled for 1 h. After impregnation, the preform was taken out and centrifuged, then it was heated to 353 K and cured for 2 h. After curing, the preform was carbonized up to 1273 K, 2 h under an Ar atmosphere at a rate of 2 $K \cdot min^{-1}$. Also, several cured PF blocks were carried in similar pyrolysis process to obtain C powder for the determination of C in PyC–RSiC materials.

2.2.3 Infiltrated process

Infiltrated process was mainly conducted at 2173 K

Table 1 Compositions of pre-melted alloy powder

Alloy powder composition	Serial number				
	No.1	No.2	No.3	No.4	No.5
$MoSi_2$ (wt%)	15.00	20.00	25.00	30.00	35.00
Si (wt%)	70.00	70.00	65.00	60.00	55.00
Cr (wt%)	15.00	10.00	10.00	10.00	10.00

in a graphite crucible in Ar atmosphere for 1 h, and the pre-melted alloy blocks were melted and transferred into RSiC matrix via capillary action to prepare the composites [33,34].

The obtained composites are labeled as MoSiCrX, where, X stands for the serial number of pre-melted alloy compositions.

2. 3 Characterization of the $MoSi_2(Cr_5Si_3)$–RSiC composites

Phase composition of the obtained composites was determined using an X-ray diffractometer (X'Pert PRO) with nickel filtered Cu Kα radiation produced at 40 kV and 27.5 mA, at a scanning rate of 10 $(°) \cdot min^{-1}$.

Apparent porosity and volume density of the obtained composites were measured using Archimedes method [35]. Pore size distribution was determined by mercury intrusion porosimetry (MIP, Pore Master-60, Quantachrome, USA). The He permeation characteristics of the composites were measured according to Ref. [36] using a Helium Mass Spectrometer Leak Detector (ZQJ-2000, Beijing Zhongke Keyi Co., Ltd., China).

The microstructure and element analysis of the obtained composites were performed with a scanning electron microscope (SEM FEI Quanta 200) equipped with an energy dispersive spectrometer (Oxford).

A GKZ-II servohydraulic testing machine with the indenter and holder made of dense SiC material equipped with a split furnace attachment was conducted to study the temperature dependence of mechanical properties of the obtained composites [1,37]. The load is recorded by the attached weighting sensor, at the same time, displacement sensor is used to record the displacement of material under stress, and the accuracy for both data is ±1%. All specimens were ground with diamond wheels and the tensile surfaces were polished better than 1 μm in advance; the edges of samples were beveled to avoid stress concentration during testing. A batch of five specimens were tested and the obtained values were averaged. Specimens with the size of 3 mm × 4 mm × 50 mm were used to measure the three-point flexural strength (σ_f) and elastic modulus (E_f) with a span of 30 mm and a loading rate of 0.5 $mm \cdot min^{-1}$ [1,38]. The fracture toughness (K_{IC}) of the as-prepared samples was measured by the single-edge-notched-beam (SENB) method, the size of the specimens was 4 mm (height) × 2 mm (width) × 35 mm (length) with a span of 15 mm and a loading velocity of 0.5 $mm \cdot min^{-1}$, and the notches were incised

in the middle of the samples along the height using a circular saw with a width of 0.3 mm to the depth of 1–1.5 mm [39].
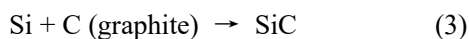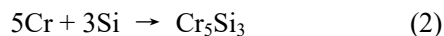
Composites with the same size and pre-treated process were used for oxidation resistance and mechanical properties test before and after oxidation at different time. The oxidation process was described as followings: samples were heated to 1373, 1473, 1573, 1673, and 1773 K at a rate of 10 K·min^{-1} and soaked 10 h at the temperature, respectively, then they were cooled down to room temperature naturally. The operation was repeated 10 cycles, and a batch of five specimens was kept every cycle for weight change and mechanical property measurement. All operations were performed in static air using a $MoSi_2$ heating furnace, and the temperature accuracy was estimated to be ±10 K. For comparison, RSiC matrix was pre-treated and oxidized at the same condition.

3 Results and discussion

3.1 Microstructure, composition, and porosity of the $MoSi_2(Cr_5Si_3)$–RSiC composites

3.1.1 *Phase identification of the $MoSi_2(Cr_5Si_3)$–RSiC composites*

XRD patterns of RSiC, PyC powder, $MoSi_2$, and $MoSi_2(Cr_5Si_3)$–RSiC composites are shown in Fig. 1. Compared with the standard XRD spectra, the main compositions of RSiC and $MoSi_2$ are clearly 6H–SiC and 6H–$MoSi_2$, and PyC is amorphous [1,40]. The $MoSi_2(Cr_5Si_3)$–RSiC composites mainly compose of 6H–SiC, hexagonal $MoSi_2$, and tetragonal Cr_5Si_3, a small amount of 6H $Mo_{4.8}Si_3C_{0.6}$ are also found, newly formed Cr_5Si_3 and $Mo_{4.8}Si_3C_{0.6}$ are derived from the reaction of $MoSi_2$, PyC, Cr, and Si. The possible reactions are as follows [1,21,27]:

$$24MoSi_2 + 36C \rightarrow 5Mo_{4.8}Si_3C_{0.6} + 33SiC \quad (1)$$

$$5Cr + 3Si \rightarrow Cr_5Si_3 \quad (2)$$

$$Si + C \,(graphite) \rightarrow SiC \quad (3)$$

Also, it can be seen clearly that weight ratios between $MoSi_2$, Cr_5Si_3, and $Mo_{4.8}Si_3C_{0.6}$ possess different values in different composites as the intensity ratios of the corresponding peaks in XRD patterns exhibit different values for different composites [41], which may affect the microstructure of the composites as the infiltrated phase $MoSi_2$, Cr_5Si_3, and $Mo_{4.8}Si_3C_{0.6}$ possess different
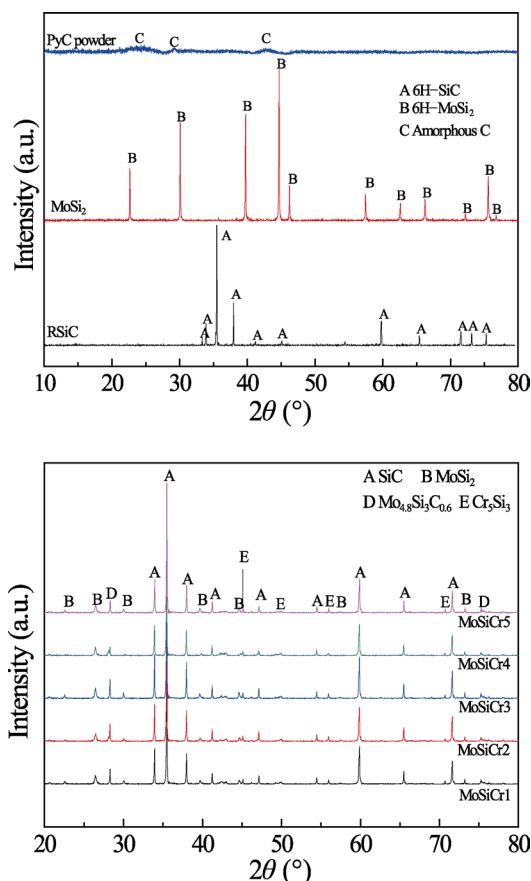

Fig. 1 XRD patterns of RSiC, PyC, $MoSi_2$, and $MoSi_2(Cr_5Si_3)$–RSiC composites.

physical properties, such as coefficient of thermal expansion (CTE), melting point (m.p.) [14,42].

3.1.2 *Porosity characteristic and volume density of the $MoSi_2(Cr_5Si_3)$–RSiC composites*

Apparent porosity and volume density of RSiC, PyC–RSiC, and $MoSi_2(Cr_5Si_3)$–RSiC composites measured via Archimedes method [43–45] are listed in Table 2. It can be seen that the apparent porosity of PyC–RSiC is slight lower than that of RSiC, whereas its volume density is higher, owing to the PyC derived from PIP existing on the pore surface of RSiC, thereby decreasing the porosity and increasing the density of RSiC matrix [31].

As for the composites, it can be seen clearly that with the increase of $MoSi_2$ content in pre-melted alloy powder (Table 1), the apparent porosity of the corresponding composites increases while that of volume density decreases. MoSiCr1 composites possess the minimum apparent porosity (0.18%) and maximum volume density (3.19 g·cm^{-3}), respectively, suggesting that PIP–AAMI method can prepare dense $MoSi_2(Cr_5Si_3)$–RSiC composites when infiltrated at 2173 K, which is about

Table 2 Data of porosity properties, He permeation rate, and volume density of the samples

Sample	RSiC	PyC–RSiC	MoSiCr1	MoSiCr2	MoSiCr3	MoSiCr4	MoSiCr5
Apparent porosity (%)	18.62	17.40	0.18	0.54	0.68	2.28	2.37
Average pore diameter (μm)	90.30	—	29.80	24.40	27.50	29.60	30.26
Volume density (g·m^{-3})	2.61	2.62	3.19	3.16	3.13	3.10	3.07
He permeation rate (Pa·m^3·s^{-1})	—	—	5.5×10^{-9}	2.3×10^{-9}	6.5×10^{-9}	4.2×10^{-8}	8.3×10^{-8}

223–273 K lower than that of simple MI process [31].

The average pore size of RSiC is 90.2 μm (Fig. 2 and Table 2), while values for $MoSi_2(Cr_5Si_3)$–RSiC composites range from 24.4 to 30.26 μm, suggesting that infiltrated phases are moved into pores of RSiC matrix to reduce the pore size of it, also the composites possess the lower pore volume [46], which exhibits these pores are not through holes and only exist on the surface of the composites. Values of He permeation rate of the composites are determined according to Ref. [36] and are also listed in Table 2. It can be seen that the obtained composite exhibits a lower He permeation value, as compared to Dabir *et al*. [47], supporting the result that the obtained composites are dense and without through holes, which is consist with the lower porosity obtained by Archimedes method and low pore volume via mercury intrusion porosimetry (Table 2).

Given that pre-melted alloy phase exhibits an excellent wettability with RSiC matrix at about 2173 K [34], it can easily diffuse into RSiC and fill in the pore via capillary action, producing a dense $MoSi_2(Cr_5Si_3)$–RSiC composite [1,34]. As we know that $MoSi_2$ owns the highest melting point among the three components in pre-melted alloy powder ($MoSi_2$ 2303 K, Si 1683 K, and Cr 2130 K) [1,48]. The viscosity and mobility of the pre-melted alloy phase decrease with the increase of $MoSi_2$ content at infiltrated temperature (2173 K),
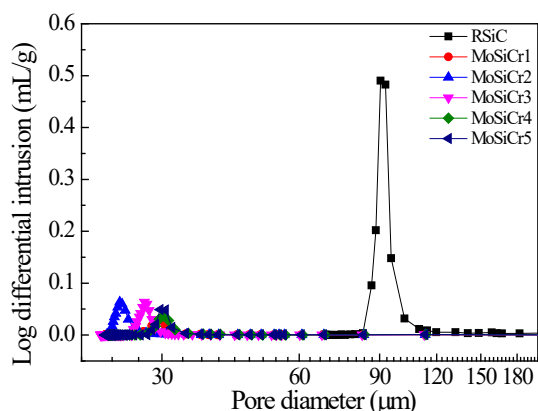

Fig. 2 Pore size distribution and average pore size of the RSiC and $MoSi_2(Cr_5Si_3)$–RSiC composites determined by mercury intrusion porosimetry.

producing an increase of the apparent porosity in the composites [49,50]. Variety of volume density depends on not only the porosity but also the composition of the composites, as the difference of theoretical densities for SiC (3.2 g·cm^{-3}), $MoSi_2$ (6.5 g·cm^{-3}), Cr_5Si_3 (5.87 g·cm^{-3}), and $Mo_{4.8}Si_3C_{0.6}$ (7.89 g·cm^{-3}), and their contents in different composites [14,42].

3.1.3 Microstructure characterization of the $MoSi_2(Cr_5Si_3)$–RSiC composites

Cross-sectional SEM images of RSiC, PyC–RSiC, and $MoSi_2(Cr_5Si_3)$–RSiC composites derived from different pre-melted alloy compositions are shown in Fig. 3.

RSiC exhibits a typical 3D interconnected porous structure in Fig. 3(a). In Figs. 3(b) and 3(b1), it can be clearly seen that PyC derived from PIP process uniformly covers on the surface of RSiC particle and combines well with it, the thickness of PyC layer ranges between 0.33 and 0.35 μm [31]. As shown in Fig. 3(c), the obtained composites exhibit a 3D interconnected network structure, both SiC phase (gray part) and infiltrated phases (white part) are continuous and 3D interpenetrating throughout the entire body of the composites [1].

As shown in Figs. 3(c1) and 3(c2), different composites exhibit different interface combinations, for MoSiCr1 and MoSiCr2 (Fig. 3(c1)), no micro-crack is observed between RSiC matrix and infiltrated phase; while for MoSiCr3, MoSiCr4, and MoSiCr5 (Fig. 3(c2)), a clear micro-crack exists, suggesting that different compositions of infiltrated phase (i.e., different weight ratios of $MoSi_2$, Cr_5Si_3, and $Mo_{4.8}Si_3C_{0.6}$) could produce different interface combination in the composites [14,31,42].

Figure 3(c3) displays the interface line-scan EDS spectra of Fig. 3(c1). Both Mo and Cr diffuse into the newly formed SiC to form the $Mo_{4.8}Si_3C_{0.6}$ phase and Cr_5Si_3 phase, and produced via the reaction of $MoSi_2$ with PyC, Cr, and Si, etc., as listed in Eqs. (1)–(3).

Namely, PIP process can modify the interface combination between RSiC matrix and infiltrated phases through the interfacial diffusion reaction in the composites, as compared to that of $MoSi_2$–RSiC composites prepared via simple MI process [1,2,31], which helps to improve

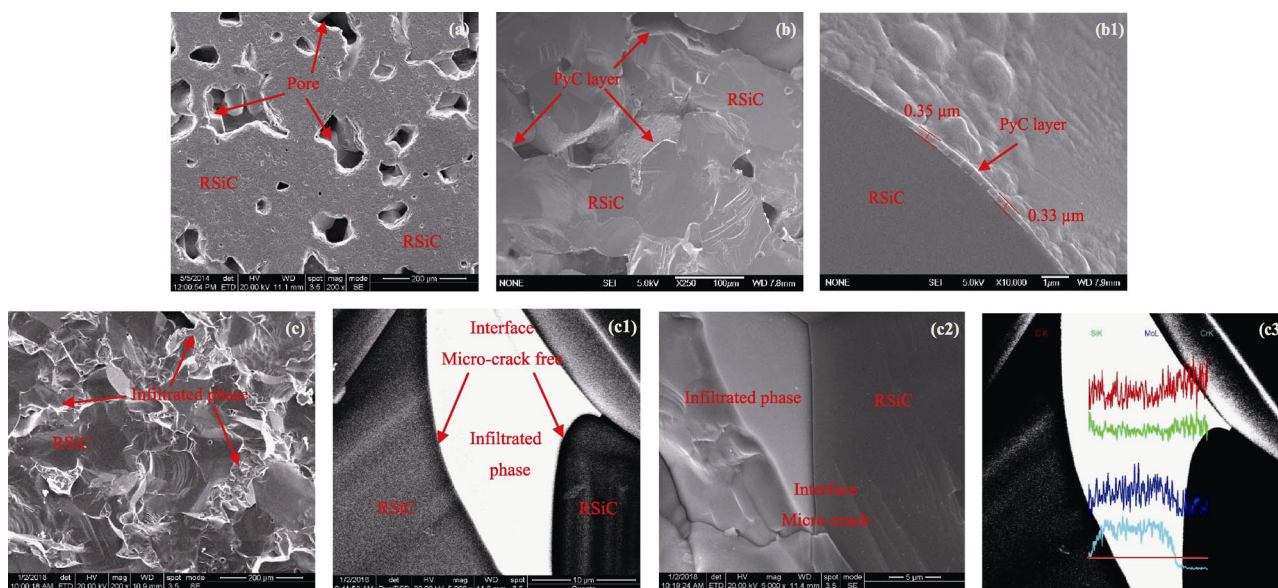**Fig. 3** Cross-sectional SEM images of RSiC, PyC–RSiC, and MoSi$_2$(Cr$_5$Si$_3$)–RSiC composites: (a) RSiC (fracture polished, low resolution), (b) PyC–RSiC (fracture, low resolution), (b1) PyC–RSiC (high resolution), (c) type MoSi$_2$(Cr$_5$Si$_3$)–RSiC composites (fracture, low resolution), (c1) MoSiCr1 and MoSiCr2 (fracture, high resolution), (c2) MoSiCr3, MoSiCr4, and MoSiCr5 (fracture, high resolution), and (c3) interface line-scan EDS spectra of (c1).

the oxidation resistance and mechanical properties of the composites under oxidized atmosphere [2].

3.2 Oxidation behavior and mechanical property variety of the MoSi$_2$(Cr$_5$Si$_3$)–RSiC composites during high-temperature oxidation

3.2.1 *Oxidation behavior of the MoSi$_2$(Cr$_5$Si$_3$)–RSiC composites at 1773 K*

Plots of the oxidation weight loss for RSiC and MoSi$_2$(Cr$_5$Si$_3$)–RSiC composites vs. time are shown in Fig. 4. The weight of samples increases with the extension of oxidation time, and all trends exhibit parabolic behavior [51]. The weight gain rate of the MoSi$_2$(Cr$_5$Si$_3$)–RSiC composites is much lower than that of RSiC, indicating that the composites possess improved oxidation resistance [51]. This improvement is mainly attributed to the acute decrease in porosity of RSiC and the outstanding oxidation resistance of the infiltrated phases [2]. Moreover, MoSiCr2 possesses the lowest weight gain of 0.1630 mg·cm^{-2}, about 78% lower than that of RSiC matrix after 100 h oxidation, which can be due to the excellent interface combination in the composites, as shown in Fig. 3(c1).

3.2.2 *Oxidation kinetics analysis of the MoSi$_2$(Cr$_5$Si$_3$)–RSiC composites*

In order to analyze the oxidation kinetics of the

composites, oxidation behavior of MoSiCr2 sample and RSiC (for comparison) at different temperatures for different time was conducted [52]. Plots of the oxidation weight loss for RSiC and MoSiCr2 composites vs. time and temperatures are shown in Fig. 5. The weight of both samples increases with the increase in oxidation time and temperature, and all trends exhibit parabolic behavior. The weight gain rate of MoSiCr2 samples is much lower than that of RSiC regardless of temperatures, once again indicating that the composites possess improved oxidation resistance.

Square of weight change per unit area vs. the oxidation time at different temperature of RSiC and MoSiCr2 samples is shown in Fig. 6, the square of weight
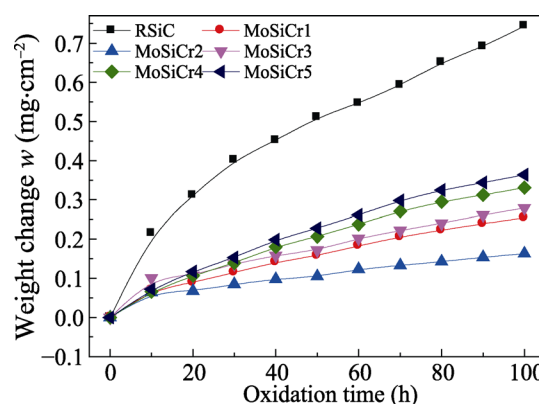

Fig. 4 Oxidation weight loss of the RSiC and MoSi$_2$(Cr$_5$Si$_3$)–RSiC composites vs. time at 1773 K.
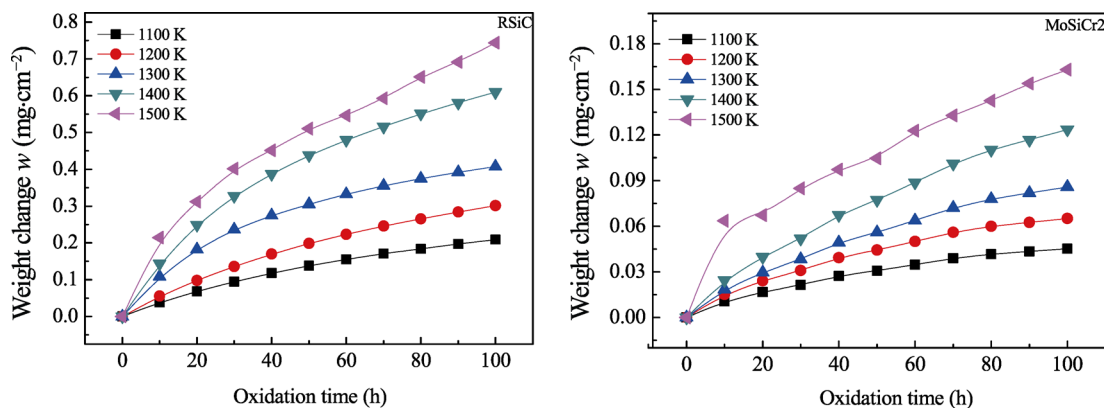
Fig. 5   Oxidation weight loss of the RSiC and MoSi$_2$(Cr$_5$Si$_3$)–RSiC composites versus time and temperature.
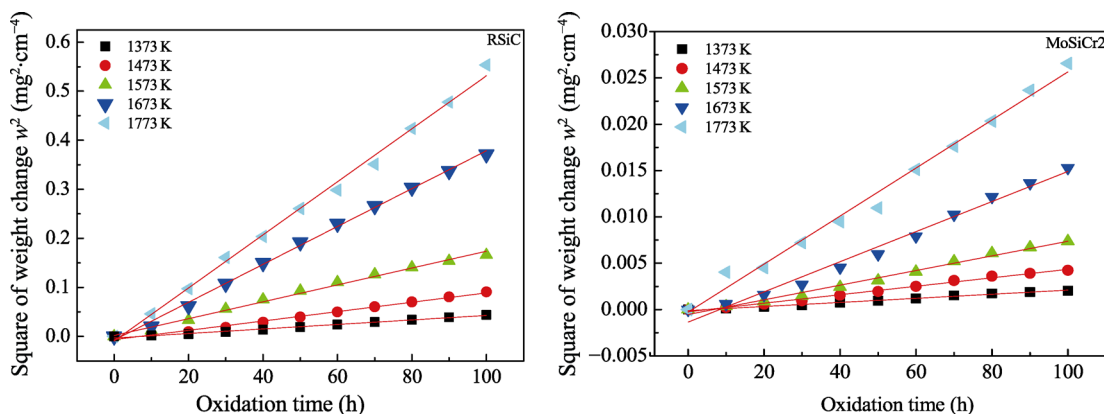

Fig. 6   Square of weight change per unit area vs. the oxidation time and temperature of RSiC and MoSi$_2$(Cr$_5$Si$_3$)–RSiC composites.

change per unit area for both samples is proportional to the oxidation time at a fixed temperature, and slope of the line represents the rate constant of sample oxidation at a fixed temperature [53]. The corresponding rate constants (k) are listed in Table 3, which are calculated using Eq. (4) as follows [53]:

$$w^2 = kt + b \approx kt \tag{4}$$

where w is the weight change per area (mg/cm^2), t is the oxidation time, and b is a constant. As shown in Table 3, the value of k for RSiC is nearly two orders of magnitude higher than that of the composites at the same temperatures, which also demonstrates the improvement of oxidation resistance for the composites.

Relationship between the reaction rate constant and temperature follows the Arrhenius equation Eq. (5) [54].

$$\ln k = \ln A - \frac{E_a}{R}\frac{1}{T} \tag{5}$$

where A is the pre-exponential factor, E_a is the apparent activation energy (kJ/mol) of the oxidation reaction in RSiC and MoSi$_2$(Cr$_5$Si$_3$)–RSiC composites, T is the absolute temperature (K), and R is the gas constant (8.314 J·mol^{-1}·K^{-1}). By changing Eq. (4) and substituting it into Eq. (5), Eq. (6) is obtained as follows:

$$\ln w^2 = \ln A + \ln t - \frac{E_a}{R}\frac{1}{T} \tag{6}$$

For the experimental conditions, value of ($\ln A + \ln t$) is constant. A set of Arrhenius curves for different samples is obtained by plotting $\ln w^2$ vs. $1/T$ (data of w

Table 3   Rate constant k and correlation coefficient r for samples oxidized at different temperatures

Samples	RSiC					MoSiCr2				
Temperature (K)	1373	1473	1573	1674	1773	1373	1473	1573	1674	1773
k ($\times 10^{-4}$)	4.606	9.552	17.234	38.627	54.123	0.081	0.168	0.530	1.625	3.167
r	0.991	0.991	0.992	0.997	0.996	0.991	0.991	0.988	0.983	0.988

and T are obtained from Fig. 5), the values of E_a are obtained from the slopes of the curves.

The Arrhenius curves of RSiC and MoSiCr are shown in Fig. 7, and the extracted values of E_a are also displayed in Fig. 7. It can be seen clearly that E_a value for high-temperature oxidation reaction of RSiC is only 128.04 kJ/mol, much lower than that of MoSiCr2 (193.86 kJ·mol^{-1}).

3.2.3 Composition and microstructure evolution during the oxidation process of the MoSi$_2$ (Cr$_5$Si$_3$)–RSiC composites

Figure 8 shows XRD patterns of MoSiCr2 composites oxidized at 1773 K for different durations (only oxides are labeled). It can be seen that amorphous SiO$_2$ and Cr$_2$O$_3$ appear after 20 h oxidation, and no MoO$_3$ is observed [2,55]. Cristobalite-SiO$_2$ and rhombohedral-Cr$_2$O$_3$ peaks are observed after 40 h of oxidation, the intensity of them increases with the oxidation time. Also, the peak intensity of SiC, MoSi$_2$, Mo$_{4.8}$Si$_3$C$_{0.6}$, and Cr$_5$Si$_3$ decreases during the entire process, and peak of Mo$_{4.8}$Si$_3$C$_{0.6}$ ($2\theta \approx 28.25°$) disappears after 40 h of oxidation. The main chemical reactions occurred at this process were as Eqs. (7) and (8).
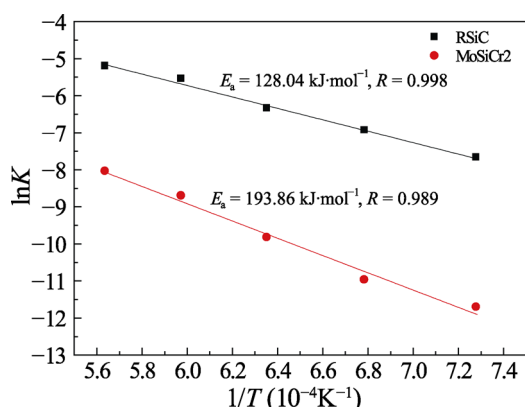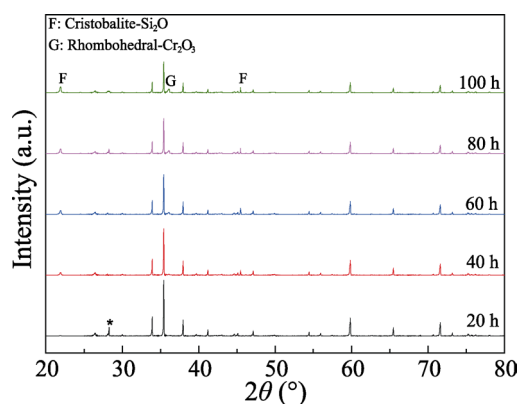
$$SiC(s) + \frac{3}{2}O_2(g) \rightarrow SiO_2(s) + CO(g) \qquad (7)$$

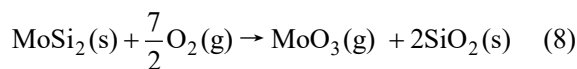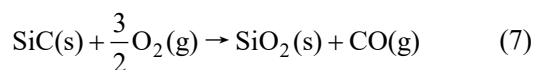$$MoSi_2(s) + \frac{7}{2}O_2(g) \rightarrow MoO_3(g) + 2SiO_2(s) \quad (8)$$

Figure 9 shows SEM images of the surface and fracture of RSiC and MoSi$_2$(Cr$_5$Si$_3$)–RSiC composites oxidized at 1773 K for 100 h. Many micro-cracks can be observed existing in flat SiO$_2$ film on RSiC surface (Fig. 9(a)), due to the transition of amorphous SiO$_2$ into cristobalite SiO$_2$ upon cooling. These micro-cracks turn to be closed when reheated. In addition, the CTE exists a mismatch between the oxidation product of SiO$_2$ (CTE$_{SiO_2, cristobalite}$ = 0.55×10^{-6} K^{-1}) and RSiC (CTE$_{RSiC}$ = $(4.8 - 5.2) \times 10^{-6}$ K^{-1}) during the cyclic heating and cooling process [2]. When cracks propagate deeply into the material, they promote oxidation and degrade the other properties of RSiC.

As for MoSiCr2, although the oxide film surface is rough, no cracks are observed (Fig. 9(a1)). The XRD spectrum indicates the existence of SiO$_2$ and Cr$_2$O$_3$ phases, and no MoO$_3$ (Fig. 8). As we know that the boiling point of MoO$_3$ is 1423 K, it would be evaporated during oxidation process as soon as it is formed [2,55]. The evaporation of MoO$_3$ and CO$_2$ (or CO) can produce a rough but dense film surface that helps to relax the thermal stress caused by the CTE mismatch between RSiC matrix, the formed oxides of SiO$_2$ (cristobalite), and Cr$_2$O$_3$ (CTE = 8.28×10^{-6} K^{-1}) [56].

Figures 9(b) and 9(c) indicate that the oxidation of RSiC occurs not only on the external surface but also on the internal surface, and the oxide film has a thickness of approximately 4.0 μm. Figures 9(b1) and 9(c1) indicate that the internal surfaces of MoSiCr2 composites exhibit minimal oxidation and no oxide film is formed, the oxidation reaction only occurs on the external surface.

The thicknesses of oxide film on the external surface of RSiC and the composites at different oxidation time are presented in Table 4 (determined by the SEM images). It indicates that the thickness of the oxide film increases with the extension of oxidation time, and the thickness of RSiC sample is much lower than that of the composites. Among five kinds of composites, the thickness slightly decreases then increases with the increase of MoSi$_2$ content in pre-melted alloy compositions (Table 1).
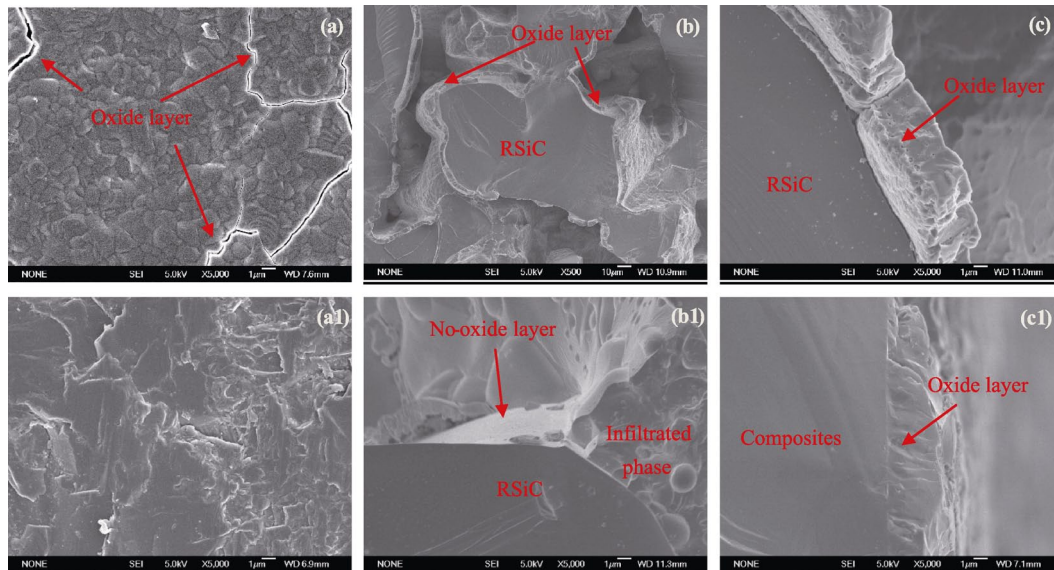
Fig. 7 Arrhenius curves of RSiC and MoSiCr2 composites.

Fig. 8 XRD patterns of the MoSi$_2$(Cr$_5$Si$_3$)–RSiC composites oxidized at 1773 K at different times.

Fig. 9 Microstructure of surface and fracture of RSiC and MoSi$_2$(Cr$_5$Si$_3$)–RSiC composites oxidized at 1773 K for 100 h: (a) RSiC (surface), (b) RSiC (fracture interior), (c) RSiC (fracture exterior), (a1) MoSiCr2 (surface), (b1) MoSiCr2 (fracture interior), and (c1) MoSiCr2 (fracture exterior).

Table 4 Thickness of the oxide layer on the surface of RSiC and MoSi$_2$(Cr$_5$Si$_3$)–RSiC composites oxidized at 1773 K

	Oxidation time (h)	20	40	60	80	100
Thickness (μm)	RSiC	1.68	2.43	2.94	3.50	4.00
	MoSiCr1	2.27	3.62	4.70	5.72	6.52
	MoSiCr2	1.72	2.49	3.15	3.67	4.18
	MoSiCr3	2.76	4.06	5.17	6.16	7.16
	MoSiCr4	2.73	4.62	6.10	7.57	8.48
	MoSiCr5	3.01	5.09	6.70	8.32	9.33

Based on Figs. 4 and 9, and Table 4, it is easy to see that higher weight gain rate of RSiC is due to the oxidation occurred on both the interior and exterior surfaces, and the lower weight gain rate of the composites is attributed to the reduced surface exposed to oxygen because the pores in RSiC are filled by infiltrated phases, allowing the oxidation reaction only occurs on the exterior surface.

3.2.4 Mechanical variety of the MoSi$_2$(Cr$_5$Si$_3$)–RSiC composites during high-temperature oxidation process

Figure 10 shows the room-temperature flexural strength and elastic modulus of RSiC and MoSi$_2$(Cr$_5$Si$_3$)–RSiC composites as functions of oxidation time to air at 1773 K. It can be clearly seen that values of σ_f and E_f for the composites increase and then decrease with the increase of MoSi$_2$ content in pre-melted alloy powder,
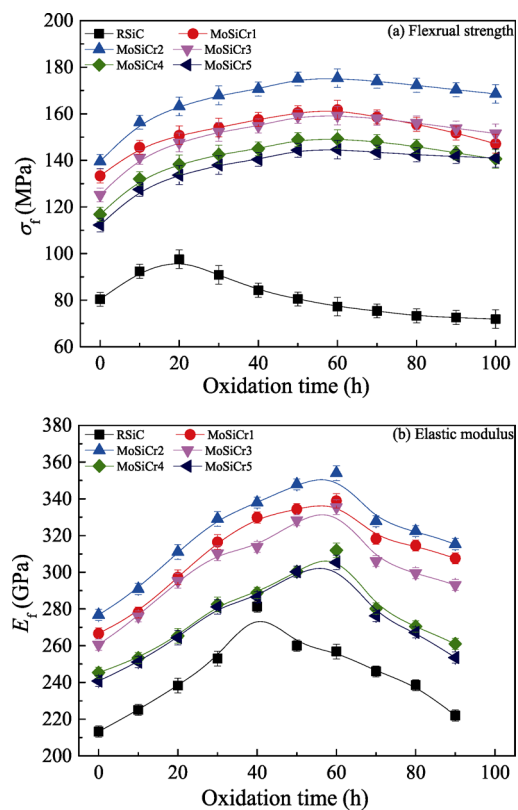

Fig. 10 Room temperature mechanical properties vs. oxidation time of RSiC and MoSi$_2$(Cr$_5$Si$_3$)–RSiC composites at 1773 K.

and MoSiCr2 possesses the highest values of 139.54 MPa (σ_f) and 276.77 GPa (E_f), improvement of 73.73% and 29.77% compared with that of RSiC, respectively; these

values are also higher than that of composites prepared via MI and PIP−MI process [1,2].

In addition, the mechanical properties of samples all firstly increase and then decrease with the increase of the oxidation time, while the maximum values for these samples are observed at different time: for RSiC, maximum values of σ_f (97.52 MPa) and E_f (242.16 GPa) are observed when oxidized for 20 h, improved by approximately 23.15% and 12.12% as compared with the initial values. For composites, the maximum values of σ_f and E_f are all observed when oxidized for 60 h, the corresponding values are 175.23 MPa (σ_f) and 354.03 GPa (E_f) for MoSiCr2, respectively, these values improve by approximately 25.22% and 32.21% when compared to the original data. Furthermore, even oxidized for 100 h, the mechanical properties of the composites are still higher than the initial values.

At the initial oxidation process, O_2 can react with SiC, $MoSi_2$, Cr_5Si_3, and $Mo_{4.8}Si_3C_{0.6}$ to form an amorphous SiO_2–Cr_2O_3 film, which can help to reduce the surface defect and improve the mechanical properties of the materials. With the increase of oxidation time ($\leqslant$ 40 h), the amorphous SiO_2–Cr_2O_3 film is slowly transformed into the cristobalite SiO_2 and rhombohedral Cr_2O_3 mixture films; meanwhile, the evaporation of MoO_3 and CO_2 (or CO) may produce micropores on the mixture films to relax the mismatch of CTE between RSiC, $MoSi_2$, and oxides, and also the high temperature can reduce or remove the internal thermal stress of the composites to improve the mechanical properties [1]. A further extension of oxidation time may result in the crystal growth and thickness increase of oxide layer, which has a negative role on the mechanical properties of the composites.

The combination of surface defect reduction via oxidation reaction, thermal stress relaxation in the composites, crystal growth, and thickness increase of the oxide layer results in the mechanical properties of the composites exhibiting an increasing firstly and then decreasing trend with extension of the oxidation time.

3. 4   Temperature dependence of mechanical retention properties of the MoSi₂(Cr₅Si₃)–RSiC composites

Experimental flexural stress–strain curves of MoSiCr2 tested in air at different temperatures are shown in Fig. 11. All curves display an approximately linear behavior, regardless of the temperature, namely a brittle fracture. As we know that the brittle-ductile transition temperature
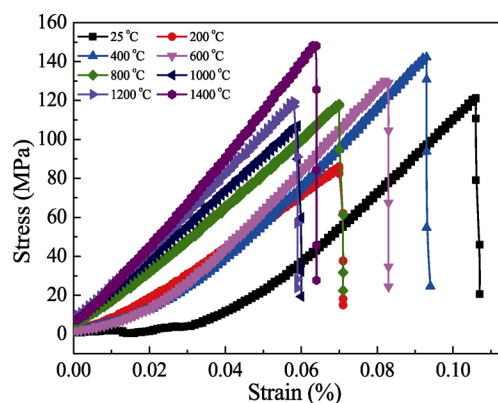

Fig. 11   Flexural stress–strain curves of the MoSi₂(Cr₅Si₃)–RSiC composites tested at different temperatures.

(BDTT) of $MoSi_2$ is in the vicinity of 1273 K, and it will occur a plastic deformation above this temperature [57], while the rigid framework of RSiC and the special 3D interpenetrating network of the composites can confine this deformation [2,58], resulting in a brittle fracture behavior for the MoSi₂(Cr₅Si₃)–RSiC composites.

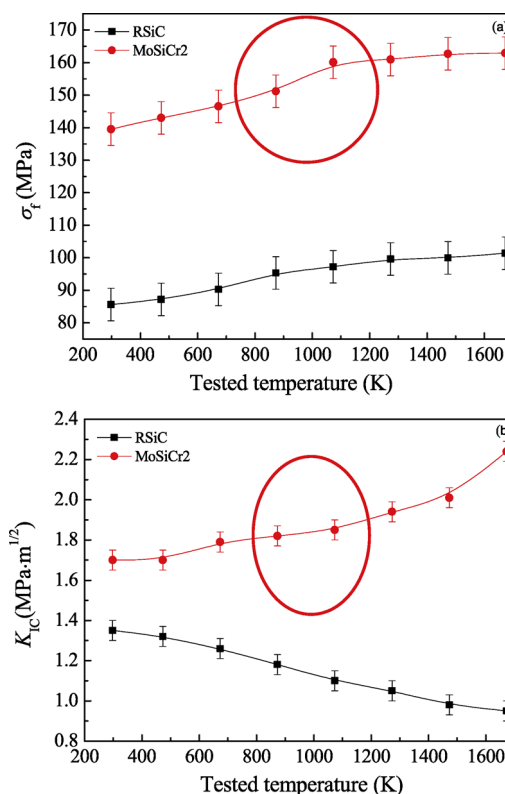Figure 12 displays the mechanical properties of RSiC and MoSi₂(Cr₅Si₃)–RSiC composites as a function of

Fig. 12   Temperature dependence of mechanical properties for RSiC and MoSi₂(Cr₅Si₃)–RSiC composites: (a) flexural strength and (b) fracture toughness.

tested temperatures. With the increase of temperature, both σ_f and K_{IC} values of the composites increase, especially when temperature increases from 1173 to 1373 K, values of σ_f and K_{IC} exhibit a clear increase (red circle in Figs. 12(a) and 12(b), respectively), which may result from the fragile–ductile transition of MoSi2, similar with research results of Refs. [2,59].

As for σ_f value of MoSiCr2, it increases from 139.54 (RT) to 162.90 MPa (1673 K), exhibiting the improvement of 16.7%, and for K_{IC}, the value of MoSiCr2 reaches 2.24 MPa·m$^{1/2}$ (1673 K), increasing 31.7% compared with that of RT value.

4 Conclusions

(1) A nearly full dense $MoSi_2(Cr_5Si_3)$–RSiC composite exhibiting a 3D interpenetrated network structure was obtained via a combined PIP–AAMI process. XRD pattern confirmed that the primary compositions of the composites were 6H–SiC, hexagonal MoSi2, tetragonal Cr_5Si_3, and a small amount of $Mo_{4.8}Si_3C_{0.6}$; interface combination of the composites mainly depended on the compositions' ratio of the infiltrated phases.

(2) Weight gain rate of the composites was much lower than that of RSiC, and MoSiCr2 possessed the lowest value of 0.1630 mg·cm^{-2}, about 78% lower than that of RSiC matrix after oxidation at 1773 K for 100 h. The infiltrated phases filling the pores of RSiC primarily contributed to the improvement for impeding the occurrence of oxidation reaction on the internal surfaces of the composites.

(3) MoSiCr2 possessed the highest mechanical properties of 139.54 MPa (σ_f) and 276.77 GPa (E_f), improvement of 73.73% and 29.77% compared with that of RSiC, respectively. Also, the mechanical properties of the composites increased first and then decreased with the extension of oxidation time, due to the co-operation effects of surface defect reduction via the oxidation reaction and thermal stress relaxation in the composites, crystal growth and thickness increase of the oxide film.

(4) With the increase of the tested temperatures, both flexural strength and fracture toughness of the composites increased. The σ_f value of MoSiCr2 increased from 139.54 MPa (RT) to 162.90 MPa (1673 K), exhibiting an improvement of 16.7%, and for K_{IC}, the value of MoSiCr2 reached to 2.24 MPa·m$^{1/2}$ at 1673 K, showing an improvement of 31.7% compared with the RT value.

References

[1] Gao PZ, Xu MY, Yuan Z, *et al*. Temperature dependence of the mechanical and thermal expansion behaviors of MoSi2-RSiC composites with a three-dimensionally (3D) interpenetrated network structure. *J Alloys Compd* 2018, **731**: 1103–1111.

[2] Xie W, Gao PZ, Li DY, *et al*. Detailed electrical and mechanical retention characteristics of MoSi2-RSiC composites exhibiting three-dimensional (3D) interpenetrated network structure during long-term high-temperature oxidation process. *Ceram Int* 2016, **42**: 5873–5884.

[3] Simonenko EP, Simonenko NP, Shembel NL, *et al*. Polymer technology of porous SiC ceramics using milled SiO2 fibers. *Russ J Inorg Chem* 2018, **63**: 574–582.

[4] Li J, Zhuang XG, Monfort E, *et al*. Utilization of coal fly ash from a Chinese power plant for manufacturing highly insulating foam glass: implications of physical, mechanical properties and environmental features. *Constr Build Mater* 2018, **175**: 64–76.

[5] Du BC, Qiu Y, He YL, *et al*. Study on heat transfer and stress characteristics of the pressurized volumetric receiver in solar power tower system. *Appl Therm Eng* 2018, **133**: 341–350.

[6] Guo WM, Xiao HN, Lei HB, *et al*. Effect of SiO2 content on the microstructure and consolidation mechanism of recrystallized silicon carbide. *J Ceram Proc Res* 2011, **12**: 682–687.

[7] Lei HB, Xiao HN, Guo WM, *et al*. Effect of high temperature oxidation on the fracture strength of recrystallized silicon carbide. *J Chin Ceram Soc* 2010, **38**: 1519–1522. (in Chinese)

[8] Qiao ZJ, Zhou T, Kang JL, *et al*. Three-dimensional interpenetrating network graphene/copper composites with simultaneously enhanced strength, ductility and conductivity. *Mater Lett* 2018, **224**: 37–41.

[9] Liu J, Wu JY, Binner J. Cutting resistance of metal-ceramic interpenetrating composites. *Ceram Int* 2017, **43**: 2815–2823.

[10] Wang DM, Zheng ZX, Lv J, *et al*. Enhanced thermal conductive 3D-SiC/Al-Si-Mg interpenetrating composites fabricated by pressureless infiltration. *Ceram Int* 2017, **43**: 1755–1761.

[11] Kulczyk-Malecka J, Zhang X, Carr J, *et al*. Thermo-mechanical

properties of SPS produced self-healing thermal barrier coatings containing pure and alloyed MoSi₂ particles. *J Eur Ceram Soc* 2018, **38**: 4268–4275.

[12] Hsu HF, Tsai PC, Lu KC. Single-crystalline chromium silicide nanowires and their physical properties. *Nanoscale Res Lett* 2015, **10**: 50.

[13] Zhang TT, Yang XS, Miao KS, *et al*. Microstructure evolution and brazing mechanism of Ti₅Si₃/Ti₃Al composite and Ni-based superalloy joints using Ti-Zr-Cu-Ni filler alloy. *Mater Sci Eng* 2018, **713**: 28–34.

[14] Yi DQ, Liu HQ, Wang B. *Metal silicide*. Beijing, China: Metallurgical Industry Press, 2012: 6.

[15] Hao ZH, Sun W, Xiong X, *et al*. Microstructure and ablation properties of a gradient Cf/C-XSi₂-SiC(X = Mo, Ti) composite fabricated by reactive melt infiltration. *J Eur Ceram Soc* 2016, **36**: 3775–3782.

[16] Song N, Zhang HB, Liu H, *et al*. Effects of SiC whiskers on the mechanical properties and microstructure of SiC ceramics by reactive sintering. *Ceram Int* 2017, **43**: 6786–6790.

[17] Bougiouri V, Voytovych R, Rojo-Calderon N, *et al*. The role of the chemical reaction in the infiltration of porous carbon by NiSi alloys. *Scripta Mater* 2006, **54**: 1875–1878.

[18] Caccia M, Xiang CC, Narciso J, *et al*. Reactive melt infiltration as synthesis route for enhanced SiC/CoSi₂ composite materials for advanced armor systems. *Ceram Int* 2018, **44**: 13182–13190.

[19] Bhattacharya AK, Heinrich JG. Cellular molybdenum silicide/silicon carbide composites from stems of maize. *J Am Ceram Soc* 2006, **89**: 367–369.

[20] Novakovic R, Giuranno D, Caccia M, *et al*. Thermodynamic, surface and structural properties of liquid Co-Si alloys. *J Mol Liq* 2016, **221**: 346–353.

[21] Xu MY. *Study on Preparation, Characterization and Property of Metal-Carbon-Silicide-based and Metal Silicide Materials*. M.A. Thesis. Changsha, China: Hunan University, 2018.

[22] Roger J, Guesnet L, Marchais A, *et al*. SiC/Si composites elaboration by capillary infiltration of molten silicon. *J Alloys Compd* 2018, **747**: 484–494.

[23] Jiang JM, Wang S, Li W, *et al*. Preparation of 3D Cf/ZrC-SiC composites by joint processes of PIP and RMI. *Mater Sci Eng* 2014, **607**: 334–340.

[24] Calderon NR, Voytovych R, Narciso J, *et al*. Pressureless infiltration versus wetting in AlSi/graphite system. *J Mater Sci* 2010, **45**: 4345–4350.

[25] Caccia M, Amore S, Giuranno D, *et al*. Towards optimization of SiC/CoSi₂ composite material manufacture via reactive infiltration: Wetting study of Si-Co alloys on carbon materials. *J Eur Ceram Soc* 2015, **35**: 4099–4106.

[26] Voytovych R, Bougiouri V, Calderon NR, *et al*. Reactive infiltration of porous graphite by NiSi alloys. *Acta Mater* 2008, **56**: 2237–2246.

[27] Meier S, Heinrich JG. Processing-microstructure-properties relationships of MoSi₂-SiC composites. *J Eur Ceram Soc*

2002, **22**: 2357–2363.

[28] Esfehanian M, Günster J, Moztarzadeh F, *et al*. Development of a high temperature Cf/XSi₂-SiC (X = Mo,Ti) composite via reactive melt infiltration. *J Eur Ceram Soc* 2007, **27**: 1229–1235.

[29] Hu DL, Zhang F. *Ternary Alloy Phase Diagram*. Xi'an, China: Northwestern Polytechnical University Press, 1995: 63.

[30] Bhattacharyya D, Davis J, Drew M, *et al*. Characterization of complex carbide–silicide precipitates in a Ni–Cr–Mo–Fe–Si alloy modified by welding. *Mater Charact* 2015, **105**: 118–128.

[31] Lv HN. Study on electrical and thermal behavior of MoSi₂-RSiC composites. Ph.D. Thesis. Changsha, China: Hunan University, 2017.

[32] He Z, Lian PF, Song Y, *et al*. Improving molten fluoride salt and Xe135 barrier property of nuclear graphite by phenolic resin impregnation process. *J Nucl Mater* 2018, **499**: 79–87.

[33] Constantin H, Harper L, Kennedy AR. Pressure-assisted infiltration of molten metals into non-rigid, porous carbon fibre structures. *J Mater Process Technol* 2018, **255**: 66–75.

[34] Gao PZ, Zhang XL, Huang ST, *et al*. Influence of infiltration temperatures on microstructure and properties of MoSi₂(Cr₅Si₃)-RSiC composites. *J Chin Ceram Soc* 2014, **42**: 1105–1110.

[35] Liu JJ, Huo WL, Zhang XY, *et al*. Optimal design on the high-temperature mechanical properties of porous alumina ceramics based on fractal dimension analysis. *J Adv Ceram* 2018, **7**: 89–98.

[36] China-GB/T. GB/T 13979-2008 Mass spectrometer leak detector. 2008.

[37] He RJ, Qu ZL, Liang D. Rapid heating thermal shock study of ultra high temperature ceramics using an *in situ* testing method. *J Adv Ceram* 2017, **6**: 279–287.

[38] Nie GL, Bao YW, Wan DT, *et al*. Evaluating high temperature elastic modulus of ceramic coatings by relative method. *J Adv Ceram* 2017, **6**: 288–303.

[39] Cui JP, Gong ZY, Rao PG. Effect of molten zone ablated by femtosecond laser on fracture toughness of oxide ceramics. *J Eur Ceram Soc* 2018, **38**: 2440–2444.

[40] Rastegar H, Bavand-vandchali M, Nemati A, *et al*. Catalytic graphitization behavior of phenolic resins by addition of in situ formed nano-Fe particles. *Phys E* 2018, **101**: 50–61.

[41] Durdziński PT, Ben Haha M, Zajac M, *et al*. Phase assemblage of composite cements. *Cem Concr Res* 2017, **99**: 172–182.

[42] Xie W. Microstructure controling and properties of MoSi₂/RSiC composites with three-dimensional network structure. Ph.D. Thesis. Changsha, China: Hunan University, 2016.

[43] Li S, Xiong DG, Liu M, *et al*. Thermophysical properties of SiC/Al composites with three dimensional interpenetrating

network structure. *Ceram Int* 2014, **40**: 7539–7544.

[44] Wang B, Xu ZY, Lu WZ, *et al*. Effect of porous Si_3N_4 preform on the mechanical properties of Si_3N_4/Al composites with interpenetrating network structure. *Mater Sci Eng* 2014, **607**: 307–312.

[45] Gao PZ, Wang L, Huang ST, *et al*. Microstructure and mechanical properties of 3-D interpenetrated network structure $MoSi_2$-RSiC composite. *Ceram Int* 2012, **38**: 5799–5805.

[46] Queiroga JA, Nunes EHM, Souza DF, *et al*. Microstructural investigation and performance evaluation of slip-cast alumina supports. *Ceram Int* 2017, **43**: 3824–3830.

[47] Dabir S, Deng WX, Sahimi M, *et al*. Fabrication of silicon carbide membranes on highly permeable supports. *J Membr Sci* 2017, **537**: 239–247.

[48] Cao XZ, Song TY, Wang XQ. *Inorganic Chemistry*. 3rd edn. Beijing, China: Higher Education Press, 1994.

[49] Li Y, Chen WZ, Dong BS, *et al*. Effects of metalloid content on viscosity of Fe-Si-B-P-C alloy melt. *J Non-cryst Solids* 2018, **490**: 31–34.

[50] Lin ZY, Liu HQ, Li QG, *et al*. High thermal conductivity liquid metal pad for heat dissipation in electronic devices. *Appl Phys A* 2018, **124**: 368.

[51] Qu SJ, Tang SQ, Feng AH, *et al*. Microstructural evolution and high-temperature oxidation mechanisms of a titanium aluminide based alloy. *Acta Mater* 2018, **148**: 300–310.

[52] Zapata-Solvas E, Jayaseelan DD, Brown PM, *et al*. Effect of La_2O_3 addition on long-term oxidation kinetics of ZrB_2-SiC and HfB_2-SiC ultra-high temperature ceramics. *J Eur Ceram Soc* 2014, **34**: 3535–3548.

[53] Sen S, Ozdemir O, Demirkä AS, *et al*. Oxidation kinetics of chromium carbide coating produced on AISI 1040 steel by thermo-reactive deposition method during high temperature in air. *Adv Mat Res* 2012, **445**: 649–654.

[54] Department of Physical Chemistry, Tianjin University. *Physical Chemistry*. 5th edn. Beijing, China: Higher Education Press, 2009.

[55] Sun J, Fu QG, Huo CX, *et al*. Oxidation response determined by multiphase-dependent melting degree of plasma sprayed $MoSi_2$ on Nb-based alloy. *J Alloys Compd* 2018, **762**: 922–932.

[56] Wang Y, Fang HZ, Zacherl CL, *et al*. First-principles lattice dynamics, thermodynamics, and elasticity of Cr_2O_3. *Surf Sci* 2012, **606**: 1422–1425.

[57] Manukyan KV, Kharatyan SL, Blugan G, *et al*. $MoSi_2$-Si_3N_4 composites: Influence of starting materials and fabrication route on electrical and mechanical properties. *J Eur Ceram Soc* 2009, **29**: 2053–2060.

[58] Lv HN, Zhang XL, Gao PZ, *et al*. Influence of density on the microstructure, mechanical, electrical and thermal properties of recrystallized silicon carbide. *Key Eng Mat* 2016, **680**: 93–98.

[59] Jain MK, Das J, Subrahmanyam J, *et al*. Interfacial characterization in ductile refractory metals reinforced $MoSi_2$ based laminated composites. *Int J Refract Met Hard Mater* 2017, **66**: 258–270.